Numerical study of impeller-driven von Kármán flows via a volume penalization method

S Kreuzahler[1]**, D Schulz**[1]**, H Homann**[2]**, Y Ponty**[2] **and R Grauer**[1]

[1] Institut für Theoretische Physik I, Ruhr-Universität Bochum, D-44780 Bochum, Germany
[2] Université de Nice-Sophia, CNRS, Observatoire de la Côte d'Azur, BP 4229 06304 Nice Cedex 4, France
E-mail: grauer@tp1.rub.de

Abstract

Studying strongly turbulent flows is still a major challenge in fluid dynamics. It is highly desirable to have comparable experiments to obtain a better understanding of the mechanisms generating turbulence. The von Kármán flow apparatus is one of those experiments that has been used in various turbulence studies by different experimental groups over the last two decades. The von Kármán flow apparatus produces a highly turbulent flow inside a cylinder vessel driven by two counter-rotating impellers. The studies cover a broad range of physical systems including incompressible flows, especially water and air, magnetohydrodynamic systems using liquid metal for understanding the important topic of the dynamo instability, particle tracking to study Lagrangian type turbulence and recently quantum turbulence in super-fluid helium. Therefore, accompanying numerical studies of the von Kármán flow that compare quantitatively data with those from experiments are of high importance for understanding the mechanism producing the characteristic flow patterns. We present a direct numerical simulation (DNS) version the von Kármán flow, forced by two rotating impellers. The cylinder geometry and the rotating objects are modelled via a penalization method and implemented in a massive parallel pseudo-spectral Navier–Stokes solver. From the wide range of different impellers used in von Kármán water and sodium experiments we choose a special configuration (TM28), in order to compare our simulations with the according set of well documented water experiments.

Though this configuration is different from the one in the final VKS experiment (TM73), using our method it is quite easy to change the impeller shape to the one actually used in VKS. The decomposition into poloidal and toroidal components and the mean velocity field from our simulations are in good agreement with experimental results. In addition, we analysed the flow structure close to the impeller blades, a region hardly accessible to experiments. Depending on the blade geometry different vortex topologies are found. The very promising results imply that our numerical modelling could also be applied to other physical systems and configurations driven by the von Kármán flow.

S Online supplementary data available from stacks.iop.org/njp/16/103001/mmedia

Keywords: von Kármán flow, turbulence, moving boundaries, volume penalization, pseudospectral method

1. Introduction

In order to make progress in understanding strongly turbulent flows a set of standard experiments which can be used by different groups for studying different physical questions is highly desirable. The von Kármán experiment is an important example of such a standard experiment. It consists of a cylindrical vessel in which a flow is generated by the rotation of two impellers at the extremities of the vessel [1]. Studying turbulence by means of von Kármán fluid experiments has a strong tradition in the last two decades. Several teams set up such experiments with different designs in incompressible flows using water [2, 3] and air [4–7]. This type of experiments was also one of the first setups used to study Lagrangian statistics of turbulent flows [8–11], by tracking solid particles or bubbles. Recently, a helium super-fluid experiment has been built with the classic von Kármán configuration [12] to reach even higher Reynolds number, and to study the interaction of the super and classic fluid.

In the last decade, in order to gain a better understanding of the underlying processes of magnetohydrodynamic and dynamo effect, many experimental groups have investigated experiments using liquid sodium [13–16]. A very successful experiment used the von Kármán apparatus with sodium liquid (VKS) hosted in Cadarache which was able to reproduce dynamo action in a turbulent flow [17–22]. Before starting with sodium experiments, prototypes filled with water were set up. They compared and optimized different impeller designs to seek the highest kinematic dynamo growth rate [23, 24].

In this paper we focus on the purely hydrodynamic properties of the von Kármán flow driven by rotating impellers and keep the investigation of the magnetized dynamics for future work. To this end we perform direct numerical simulations (DNSs) of a von Kármán flow, thus a three-dimensional impeller-driven turbulent flow in cylindrical geometry. The geometry of rotating impellers assembled of several basic geometric objects is modelled via an immersed boundary technique (IBM) and implemented in a massive parallel pseudo-spectral Navier–Stokes solver. High resolution simulations allow for the development of a turbulent flow. This method allows the simulation of a free flow inside a confining solid object driven by rotating impellers, in contrast to previous numerical approaches with prescribed velocity fields

[23, 25], periodic domains [26–28] or volume forcings [29]. We compare our numerical results with the mentioned water experiments [30–34] to validate our numerical modelization approach. The benefit of a numerical investigation is demonstrated by studying the flow dynamics in the vicinity of impellers, a region not easily accessible experimentally. Our data reveals the existence of a coherent vortex structure in the frame of reference that co-rotates with the impellers.

2. Numerical method

2.1. Basic equations

We consider the incompressible Navier–Stokes equation

$$\frac{\partial \mathbf{u}}{\partial t} + (\mathbf{u} \cdot \nabla)\mathbf{u} = -\nabla p + \nu \Delta \mathbf{u} \tag{1}$$

with the velocity field $\mathbf{u}(\mathbf{x}, t)$, pressure p, viscosity ν. The velocity field additionally fulfills the incompressibility condition $\nabla \cdot \mathbf{u} = 0$. At the boundaries we impose a no-slip condition such that the velocity of the fluid equals the velocity of the boundary itself $\mathbf{u}|_{\text{boundary}} = \mathbf{V}_{\text{penalized}}$. It is zero on the fixed outer cylinder and equals the solid rotation velocity on the disks and the blade structures. The cylindrical wall and the moving impellers are implemented by a penalization method (see section 2.3).

2.2. The Fourier-spectral scheme

To solve the equation system a standard pseudo-spectral method is applied using the 2/3 rule for dealiasing and resolutions of 256^3 and 512^3 grid points. The time derivative on the left-hand side of the Navier–Stokes equation is discretized via a strongly stable third order Runge–Kutta method [35]. Incompressible turbulent flows have been intensively studied in a periodic box, a classical mathematical framework for theories [36] as well as for numerical simulations of isotropic and homogeneous turbulence [37, 38]. In this geometry the pseudo-spectral numerical method is the most precise global numerical method for a fixed mesh size and the success of this method is essentially due to the efficiency of the fast Fourier transform. In the present work, we use an immersed boundary method to impose no-slip boundary conditions inside the simulation domain. In this framework we lose the spectral precision near the boundaries, but we are able to design any geometry of static or moving structure while keeping the usability of a pseudo-spectral code. The implementation of the penalization boundaries and the moving impellers doubles the CPU time. The most time-consuming part of this implementation is the recalculation of the moving boundaries in each step. For future MHD simulations we expect a factor below 2, as the penalization then consumes less time compared to the solution of the basic equations. Those methods are sufficiently accurate to reproduce standard benchmarks [39] and benchmarks depending crucially on the boundary layer solution [40]. The used method will now be explained in more detail.

2.3. Penalization method

To simulate flows within a solid cylindrical boundary and moving impellers of complex shape, a penalization method is applied. For points inside the boundaries a 'pseudo' forcing term is

added to the right-hand side of the Navier–Stokes equation (1), which adjusts the velocity exactly to the prescribed value in and on the wall or the impellers. To calculate the force we use a method that was first introduced in [41, 42]. It is called direct forcing and allows to calculate the force directly from the Navier–Stokes equation without the necessity of further auxiliary parameters. To increase the precision of the boundary layers, we used a predictor for the pressure gradient [43].

As we deal with complex geometries the boundaries of the objects do not coincide with the rectangular grid. This makes it necessary to interpolate the velocity at the boundary, for which we take the volume fraction V_b occupied by the solid object into account. Regarding the volume of each cell $V_c = \Delta x \Delta y \Delta z$, the force is weighted with the factor V_b/V_c. Practically, this is performed via a Monte–Carlo method using 50 random points within each cell to calculate the volume [42]. The details of this penalization method were described and tested in another fluid context [40].

The solid rotation velocity of the impellers is simply given by the angular velocity Ω and the distance from the axis **r** as $\mathbf{V}_{\text{boundary}} = \Omega \times \mathbf{r}$. The angular velocity of the impellers can be set independently for each impeller.

2.4. Configurations of our numerical experiments

2.4.1. Numerical experiment setup. Our aim is to model a configuration similar to the von Kármán experiments in which a cylindrical vessel is filled with a liquid. The fluid is driven by two counter-rotating impellers, one on each side of the vessel. Each impeller consists of a disk on which several blades are mounted.

We create an embedded cylinder inside the periodic box, using our penalization method, with a radius $R_c = 3.0$. Though the periodicity is kept along the z axis to decrease Gibbs oscillations, the velocity at the end of the cylinder is close to zero due to the symmetry of the system. The height of the cylinder is 2π, giving an aspect ratio of the whole cylinder volume of $2\pi/R_c$. In experimental setups this height varies from 2 up to 3 cylinder radii, thus the aspect ratio of the cylinder might slightly differ from the value chosen here. The interior of this cylinder represents ∼71% of the total computing domain.

For one set of simulations we choose a very similar configuration of the curved disk-blades to the setup called 'TM28' [23] with a distance between the disks of $1.8R_c$, leading to an aspect ratio of the bulk volume equal to that in the experiment, a radius of the rotating disk of $R_d = 0.9R_c$, a height of the eight blades of $0.2R_c$ and a curvature radius of the blades of $C = 0.5R_c$. The angle of the expelled flow at the end of the blades is given by $\alpha = \arcsin\left(R_d/2C\right) \approx 1.11976 \, rad \sim 64.15 \, deg$. For a different set of simulations we choose a straight blade configuration, which is close to the 'TM70' and 'TM80' configuration [24, 31, 33], with eight blades per disk. A difference is that our disk radius is $R_d = 0.9R_c$ instead of ($R_{TM70} = 0.75R_c$, $R_{TM80} = 0.925R_c$). We call this configuration straight configuration. Here, $C = \pm\infty$ and $\alpha = 0$.

In the following we analyse these two blade geometries (TM28 curved and straight blades). The disks are always counter-rotating with the same rotation rate. Depending on the rotation direction we have two different blade curvatures (called + or −) (see figure 1).

2.4.2. Non-dimensional numbers. We have chosen six simulations to highlight our results. We vary the viscosity ν controlling the dissipative term, the rotation rate Ω of the impellers, and the
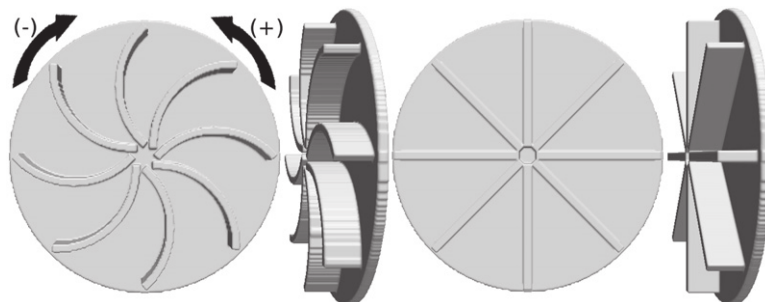
Figure 1. Simulated impellers with eight curved blades (left) and eight straight blades (right): a positive curvature, denoted (+), means that the convex side of the blade points in the turning direction of the impeller, while for a negative value, denoted (–), it is the concave side. Note that there is a small deviation from the actual experimental setup: the curved blades end exactly at the radial line of the disk, while in the experiment the endings of the blades are tangential to this line.

curvature of the blades. Of course other parameters such as the geometry of the blade, the number of blades, the difference in the rotation rate of the disks might change the topology of the flow and the quantitative results.

From our numerical data we compute a set of meaningful non-dimensional numbers (see table 1). The Reynolds number accessible with DNSs with 512^3 grid points is as usual a few orders of magnitude lower than experimental Reynolds numbers. Nevertheless, at this Reynolds number the flow is in transition to the developed turbulent state [34], thus only minor variations of global quantities should be expected for increasing *Re*. An indicator for this is the fluctuation level $\delta = \langle \mathbf{u}^2 \rangle / \langle \overline{\mathbf{u}}^2 \rangle$ defined in [44], which according to our measurements is similar to that obtained from the water experiments for synchronized rotating disks and with an annulus deviator configuration in the 'TM60' and 'TM73' setup. With asynchronous disk rotations or without annulus, this level of fluctuation could be higher (above 2.0) [44]. According to [34] the level of fluctuations first increases and then saturates with the Reynolds number *Re*, which could explain the fact that the numerical fluctuation level equals the experimental one even for a low Reynolds number.

The efficiency $E_f = U_{\max} / \Omega R_d$ of the impellers, which measures how much energy is injected into the fluid, is defined as the maximum velocity of the fluid in the bulk induced by the impeller motion. The variation of the E_f as a function of the expelled flow angle α for different experimental configurations is confronted with our numerics in figure 2(b). With a Reynolds number three orders of magnitude lower than the experiments, we nevertheless have a good agreement with the experimental efficiency. The efficiency number decreases with the same slope found in the water experiments. We noticed that our straight blade efficiency is almost identical with the 'TM70' configuration efficiency. For the positive curved blades our numerical data is closer to the 'TM60' configuration (16 blades) than to the 'TM28' (8 blades).

The ratio of the root mean square velocity and the maximum velocity of the impellers ($U_{\mathrm{rms}}/V_{\max}$) is pretty close to the 'TM28' experiment for our higher rotation rate simulation ($1.6\Omega = 2.4$).

Another non-dimensional number is the ratio of the rotation period of the impellers $T_\Omega = 1/f = \frac{2\pi}{\Omega}$ and the large eddy turn over time T_{nl}. Our simulations are in the same disk rotation regime as the experiments (see the last line of table 1) showing that there is a bit more than two large eddy turn over times during one turn of the impellers.

Table 1. Simulation quantities are compared with water experiments results from [23, 31, 33, 44] and specially the configuration 'TM28' (column 'Exp.'). The cylinder radius in the simulations is $R_c = 3.0$, with the simulation box size 2π, the disk radius is $R_d = 0.9R_c$. We collected and defined several quantities or non-dimensional numbers: ν the kinematic viscosity of water or in our simulations, Ω the rotation rate, $U_{\text{rms}} = \sqrt{2E(t)}$, U_{max} is the (spatial) maximum of the (time-averaged) mean velocity field in the bulk in the range $-0.8R_c < z < 0.8R_c$, where z = 0 is the centre of the cylinder. $L = \frac{2\pi}{\sum E(k)} \sum E(k)/k$ is the integral length scale computed with $E(K)$, the isotropic spectral density of the kinetic energy, and $T_{nl} = L/U_{\text{rms}}$ is the eddy turn over time. We used the experimental Reynolds number definition of VKE-VKS experiments $R_{\text{exp}} = \Omega R_d R_c/\nu$. To compare with numerical works, we define another Reynolds number $R_{num} = U_{rms}L/\nu$. The efficiency $E_f = U_{max}/\Omega R_c$ of the impellers states how much energy is injected into the fluid. $\delta = \langle \mathbf{u}^2 \rangle / \langle \bar{\mathbf{u}}^2 \rangle$ is the fluctuation level defined in [44]. We present also the ratios $U_{\text{rms}}/V_{\text{max}}$ and $T_\Omega/T_{nl} = \frac{2\pi U_{\text{rms}}}{\Omega L}$. Our simulations are during more than $20T_\Omega$ (turns of the impellers), which is the duration of the time average computation. The upper half of the table actually refers to the 'TM28' impeller, while the lower half (U_{rms}, U_{max}, T_{nl}, δ, $U_{\text{rms}}/V_{\text{max}}$, T_Ω/T_{nl}) refers to the 'TM60+' impeller for a general comparison of experimental and simulated impeller-driven von Kármán flows. The value for L is an estimate based on the cylinder scale R_c as the energy injection scale.

	Exp.	Curved (+)	Curved (−)	(Straight)	(+) 512	(+) 1.6Ω	(+) $\nu/2$
Grid size	—	256^3	256^3	256^3	512^3	512^3	512^3
ν	$10^{-6}\ m^2\ s^{-1}$	0.005	0.005	0.005	0.005	0.005	0.0025
Ω	$28.4628\ s^{-1}$	1.5	1.5	1.5	1.5	2.4	1.5
R_{exp}	$2.84\ 10^5$	2430	2430	2430	2430	3888	4860
R_{num}	10^5	316	404	415	308	591	732
E_f	0.64	0.50	0.698	0.635	0.504	0.502	0.504
L	0.1 m	1.6831	1.9011	1.9149	1.6349	1.9277	1.9038
U_{rms}	$\approx 1\ m\ s^{-1}$	0.9397	1.0641	1.0843	0.9429	1.5352	0.9619
U_{max}		2.268	3.143	2.859	2.268	3.616	2.268
T_{nl}	0.1 s	1.7911	1.7865	1.7660	1.7339	1.2556	1.9792
δ	1.5 − 2.2	1.452	1.433	1.487	1.40	1.519	1.519
$U_{\text{rms}}/V_{\text{max}}$	0.322	0.232	0.262	0.267	0.232	0.379	0.237
T_Ω/T_{nl}	2.207	2.34	2.338	2.3446	2.371	2.0850	2.1164

3. Mean bulk flow structure

3.1. Global flow profiles

While integrating the Navier–Stokes equations, we additionally time averaged the velocity field. The stream lines and the vector field of the mean flow $\bar{\mathbf{u}}$ are shown in figure 3(a) and figure 3(b), respectively. These images reproduce the classical images of a S2T2 type flow [45] of the von Kármán flow. For comparison, a snapshot of the enstrophy (figure 3(c)) shows interacting vortex filaments in the bulk region which is characteristic to a turbulent flow. The vorticity is produced and thus very high near the blades. This observation will be analysed in detail in section 4.
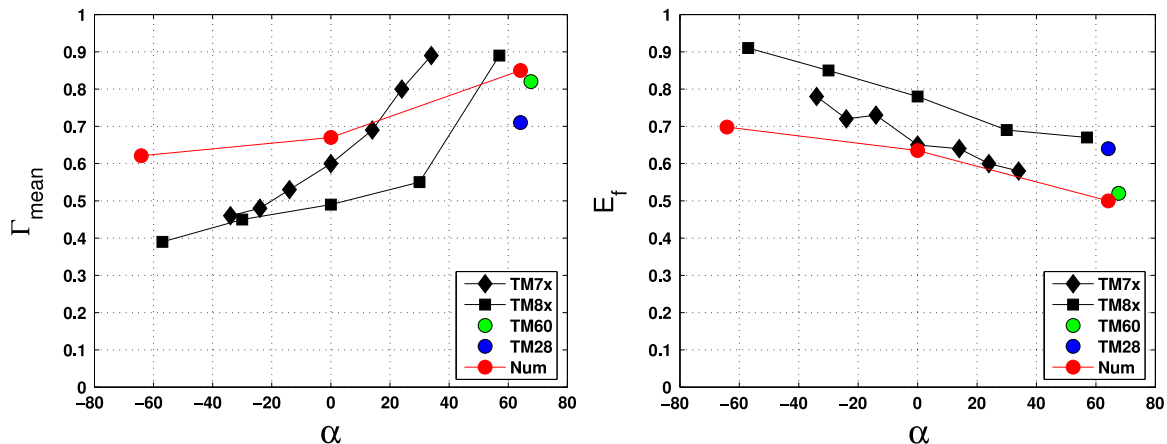
Figure 2. From different water experiment setups given in data tables (TM7x [24], TM8x [33], TM60 and TM28 [23]) and from our numerical results, we plot (left) the ratio of the poloidal and the toroidal mean velocity (Γ_{mean}) and (right) the efficiency $E_f = U_{\mathrm{max}}/\Omega R_c$ of the impellers both versus the flow expulsion angle α at the end of the blades.
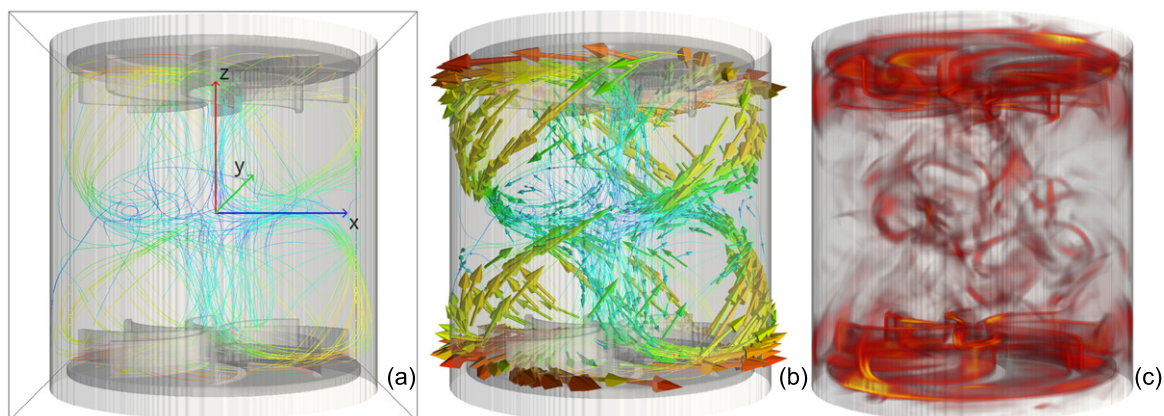

Figure 3. (a) Streamlines and (b) vector field of the time-averaged flow and (c) a snapshot of the vorticity with TM28-like (+) configuration; disk radius $0.9R_c$, 8 blades per disk with height $0.2R_c$ and curvature radius $0.5R_c$, aspect ratio of cylinder $2\pi/3$, aspect ratio of bulk 1.8, Reynolds number 2430, resolution 256^3. (Movies of the time-evolution of the fields are available in the supplementary data, available from stacks.iop. org/njp/16/103001/mmedia).

3.2. Poloidal and toroidal components

For further analysis of the simulated flows we performed a decomposition into poloidal and toroidal components of the form

$$\mathbf{u} = \mathbf{u}_{\mathrm{tor}} + \mathbf{u}_{\mathrm{pol}} = \nabla \times \left[\Psi\left(r, \theta, z\right)\mathbf{e}_z \right] + \nabla \times \nabla \times \left[\Phi\left(r, \theta, z\right)\mathbf{e}_z \right] \qquad (2)$$

with unique potential functions Ψ and Φ and the unit vector in z direction $\mathbf{e}_z$. To be precise, in the periodic box, we normally need to add a component $F(z)$ depending only on z (see [46] and
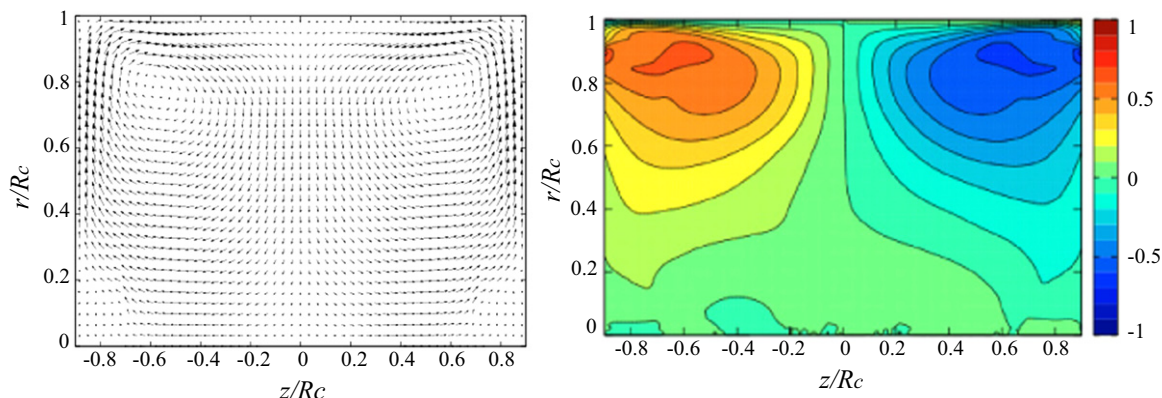
Figure 4. Projections of the poloidal (left) and toroidal (right) components generated by impellers with curved blades and positive direction, disk radius $0.9R_c$, eight blades per disk with height $0.2R_c$ and curvature radius $0.5R_c$, aspect ratio of cylinder $2\pi/3$, aspect ratio of bulk 1.8, Reynolds number 2430, resolution 256^3.

(course 2, C A Jones) [47]). Although our penalized cylinder is periodic along the z axis there is no mean flow crossing the box as the gap between the cylinder and the disks is small. We checked that F is zero (up to the numerical digit precision).

This decomposition has also been performed with the experimental data with the 'TM28' impellers, which allows a comparison of experimental and simulated data. Supposing axial symmetry around the z axis, we can compute the poloidal and toroidal two dimensional fields $\nabla \times [\Psi(r, z)\mathbf{e}_z]$ respectively $\nabla \times \nabla \times [\Phi(r, z)\mathbf{e}_z]$ (see figure 4 and compare them to figure 3 of [23]). Visually we have a good agreement, the poloidal flow consists of two large-scale vortices in the regions $z < 0$ and $z > 0$, where the toroidal components respectively point in opposite directions. Impellers with different curvature (negative curvature and straight blades) produce the same kind of flow structure. From the images it is difficult to distinguish between the different blades configurations. We therefore present in table 2 the mean and maximum velocity of the poloidal/toroidal components, all of them rescaled by their respective maximum velocity of the impellers $V_{max} = \Omega R_d$. Those values can be compared to the experimental ones [23]. Our velocities of the (+) configuration are $10\% - 20\%$ lower than the experimental data of 'TM28'. This could be explained by the fact that our efficiency coefficient is lower than the 'TM28' configuration (see figure 2 (right)), implying a smaller velocity in the central region of the vessel. We also compare the ratio of the poloidal and the toroidal velocity versus the expulsion angle of the blades α with different water experiment results [23, 24, 33]. This ratio was used to seek the dynamo onset as a control parameter. Like the efficiency the ratio Γ_{mean} for the (+) configuration is closer to the 'TM60' than the 'TM28' setup (figure 2 (left)). However we stress that our ratios have also a positive slope. Even if there is not a perfect agreement our ratios are quite close to the different experimental measurements.

3.3. Impact of viscosity and rotation speed

In order to study the impact of the viscosity and the disk rotation rate on the mean flow structure we performed additional simulations with curved impeller blades and positive turning direction. In the first of these runs we increase the resolution to 512^3 grid points (run (+) 512 in tables 1 and 2), while all other parameters are unchanged. This simulation can be seen as a convergence

Table 2. Quantities from experiments and simulations: the maximum and the mean of the poloidal and toroidal velocity and the respective ratio $\Gamma_{\max} = u_{\mathrm{pol,max}}/u_{\mathrm{tor,max}}$ and $\Gamma_{\mathrm{mean}} = u_{\mathrm{pol,mean}}/u_{\mathrm{tor,mean}}$. All the velocities are normalized by the maximum velocity of the impellers $V_{\max} = \Omega R_d$. A quantification of the poloidal and toroidal components is done by extracting the maximum and mean values in the bulk, the region $-0.8 R_c < z < 0.8 R_c$. In addition, the average torque T on the impellers has been computed for the three simulations with lower resolution and normalized using the definition of the non-dimensional torque $K_p = T (\rho R_c^5 (2\pi f)^2)^{-1}$ [34]. The values for the TM80 impeller [33] are listed for comparison with the similar straight blade configuration.

	TM28	TM80	(+)	(−)	(Straight)	(+) 512	(+) 1.6Ω	(+) $\nu/2$
$u_{\mathrm{pol,mean}}$	0.199	0.19	0.174	0.141	0.164	0.184	0.166	0.179
$u_{\mathrm{pol,max}}$	0.492		0.425	0.380	0.453	0.443	0.452	0.460
$u_{\mathrm{tor,mean}}$	0.281	0.38	0.205	0.228	0.245	0.217	0.202	0.217
$u_{\mathrm{tor,max}}$	0.691	0.74	0.535	0.824	0.708	0.538	0.530	0.509
Γ_{mean}	0.71	0.49	0.850	0.621	0.670	0.847	0.822	0.825
$\Gamma_{\max}$	0.71		0.794	0.461	0.640	0.824	0.854	0.904
K_p	–	0.111	0.0883	0.1144	0.1215	–	–	—

test. The velocities for the toroidal and poloidal component are slightly closer to the experimental values, but the non-dimensional quantities, especially the poloidal-toroidal ratios Γ, are unchanged, showing that at 256^3 grid points, our simulations are already converged.

In the second run (run (+) 1.6Ω in tables 1 and 2), the angular velocity of the impellers is increased by a factor of 1.6, while all other parameters as well as the resolution are unchanged. The Reynolds number then increases to $Re = 3888$. The listed values remain almost constant, only the ratio of the rotation period over the eddy turn over time slightly decreases and the ratio $\Gamma_{\max}$ increases slightly.

In the last run the viscosity is lowered by factor 2 (run (+) $\nu/2$ in tables 1 and 2) and the resolution is increased to 512^3 grid points. In this case the Reynolds number increases up to $Re = 4860$. Regarding all quantities obtained in the simulations, there is evidently no major influence of rotation speed and viscosity on the mean flow profile. Only the fluctuation rate δ slightly increases and the ratio $\Gamma_{\max}$ grows slightly, probably due to locally better pumping of the impellers.

The mean flow quantities that we present do not change with the rotation rate or the viscosity. This implies that the corresponding simulations are already in an asymptotic regime, where the Reynolds number has only little effect on the large-scale structure of the flow. Indeed, the range of Reynolds number numerically achieved in our work (2500–4800), is at the edge of the inertial regime of water experimental results ([34] see their figures 5 and 7). In this experimental campaign, the Reynolds number has been increased progressively by growing the rotation frequency of the disks, to explore different phases: viscous, transition and inertial regimes.
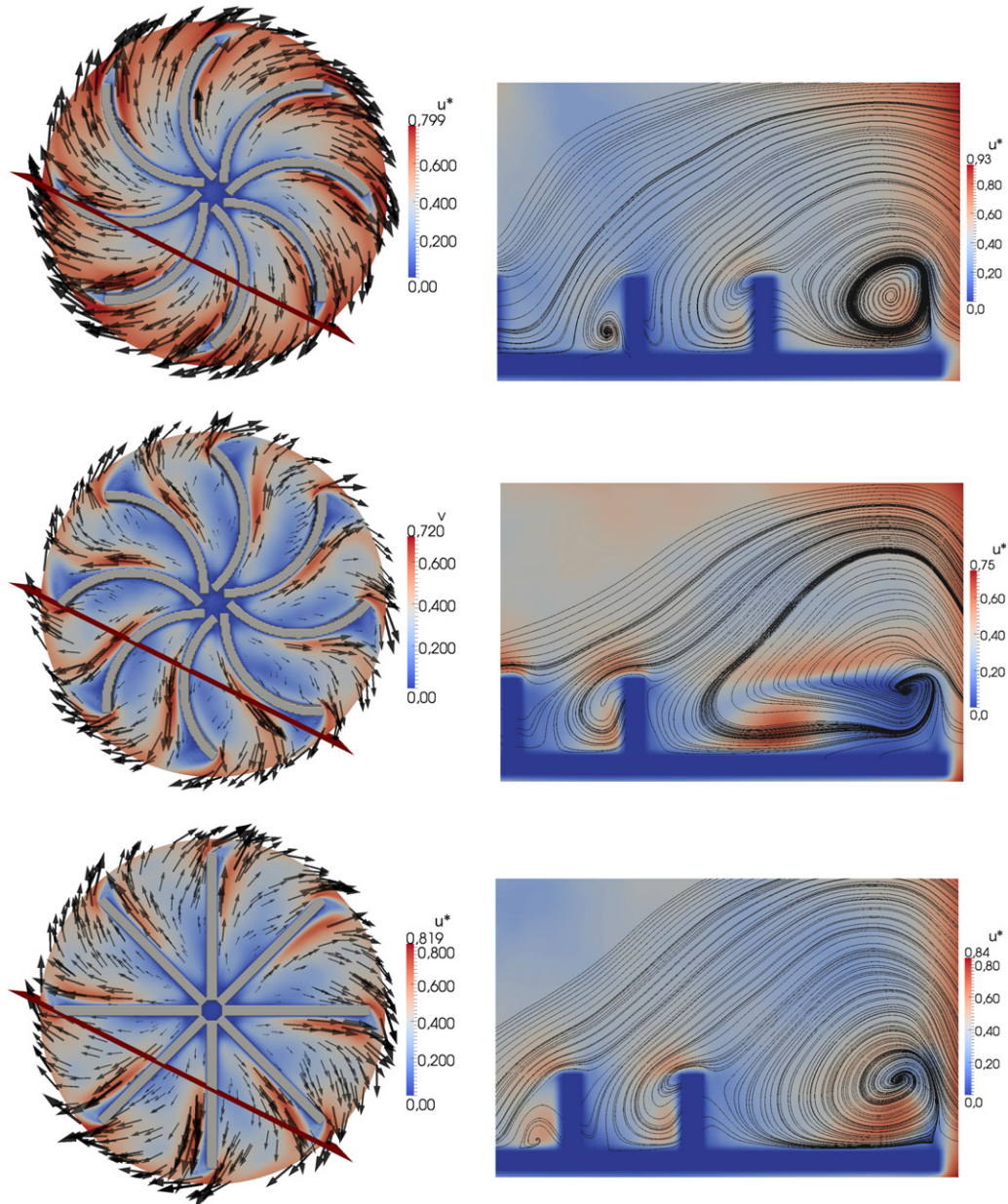
Figure 5. Visualization of the velocity field on a top view (left) and the streamlines of velocity on a transverse view (right), for our three configurations (from top to bottom (+), (−), (straight)). The velocity is averaged in time, projected on the plane, and computed in the rotating frame ($\mathbf{u}^* = \mathbf{u} - \Omega \times \mathbf{r}$). In all images, the colour map represents the magnitude of the velocity. The transverse view planes are perpendicular to the red line shown on the top view planes. Not all of the perpendicular planes associated with the red lines is plotted (only 70% of the red line of the left side). The position of the blades helps to relate the top and side views. Note that this projection of the velocity in the considered plane is not solenoidal, thus streamlines could end at the boundary, where the projected velocity tends to zero. Streamlines of the 3D flow do not enter in the solid object, but instead slide along the boundary. This behaviour is not captured by the 2D projection.

4. Local near-blade structures

4.1. Vortex generation behind blades

Besides the general flow structure imposed by the impellers, our main interest lies in the near blade flow in the frame of reference of the rotating impeller. Here, we present and analyse the structures obtained in the three different configurations ((+), (−), straight) with $n = 256$. We construct the mean flow in the rotating frame of reference by first averaging the flow each time the blades pass the same positions, which is every eighth of a turning period. As we expect to find the same mean flow at each blade we also take the spatial average for rotations around 90°. As the running time of our simulation corresponds to 20 impeller turns we were able to average over 640 realizations. The mean flow in the rotating frame is obtained from this average by subtracting a solid rotation $\mathbf{u}^* = \mathbf{u} - \Omega \times \mathbf{r}$.

To get clear pictures of the flow we consider two different planes: one parallel to the disk plane, with a view from the top and the other perpendicular to the disk (the position of the perpendicular plane is indicated by a red line in the top view (left column of figure 5). In the top view, we show the velocity projected onto the plane while its amplitude is represented by a colour map. This perspective shows how the flow is sucked in from above to the centre, moving between the blades and how it is finally expelled from the disk outwards. Just by looking at the left column of figure 5, we can easily distinguish between the different configurations, specially the (+) and the (−), where the expelled flow in the rotating frame has the same rotational direction as the disk rotation. The horizontal component represents the major part of the magnitude of the full velocity along the blade. There is clearly an acceleration from the centre to the expulsion area. The highest velocity is generally found along the pushing blade. A small sucking area is located just behind at the end of the blade.

In the perpendicular plane we decide to visualize the velocity by streamlines to highlight the topology of perpendicular flows. Note that the projected velocity is not solenoidal, thus streamlines may have an end point. In all three simulations, (right column of figure 5) the streamline plots show vortex rolls emerging directly behind the moving blade, as vortices are ripped off at the blade's edge. Those vortices appear to take most of the space between the blades. Clearly, the negative configuration (−) has a different topology than the two others. This observation agrees with the horizontal velocity in the top views. The cut along the red line allows the visualization of the mean flow vortex at different radii for different cells. In the positive configuration (+), it can be deduced that a cone vortex is produced along the pushing blade in each inter-blade cell. Those vortices are also present in the straight configuration which is, however, less clear for the negative configuration (−).

5. Discussions and perspectives

5.1. Numerical and experimental comparisons

By means of DNSs using a penalization technique we are able to reproduce the large-scale structure of experimental von Kármán flows produced by moving impellers. Our good agreement with the experimental results could be explained by the fact that the mean flow geometry and other global quantities are converging rapidly even at low Reynolds number.

The natural next step could be to seek the small scale properties of the von Kármán flow, like the studies on filaments [3, 48], effect of large scales on small scales [7] or the energy injection [49, 50]. Of course, direct numerical studies with confined flows in the full von Kármán geometry remain a challenge asking for a big increase of spatial resolution. Our modelization using the penalization could be easily used to explore different experimental setups—at least for the large-scale properties.

5.2. Vortex and dynamos

We found a characteristic outwards spiralling vortex between the blades. Note that the influence of the vortex generated around the blades is suspected to have a strong impact on the dynamo effect [51]. Some numerical results assuming a dynamo mechanism concentrated around the disk-blade structure [52, 53] have found that the magnetic mode has a dipole structure according to the experimental results. The geometry of the experimental magnetic mode cannot be explained by a mean flow dynamo only. Recent numerical studies using FLUENT ($k - \epsilon$)-RANS simulations [54] computed the α-tensor produced by the vortex dynamics, showed a switch between α^2 and $\alpha - \Omega$ dynamo types.

Despite these vortex dynamics without soft iron impellers the dynamo threshold was not achieved. The material of the impellers plays a crucial role for the efficiency of the dynamo action [55–57]. The material properties of sodium make *in situ* diagnostics very difficult. DNSs provide a unique tool to assess spatially and temporally resolved variables. The presented numerical approach in combination with a correct treatment of the magnetic properties of the solid impellers should provide a handle to address the problem of the interaction of the conducting fluid and the ferromagnetic impellers. We could also check the different dynamo onset predictions or measurements of the different configurations produced by the variation of the blade geometries or material properties [57].

5.3. Spectra and long-term dynamics

Given the temporally resolved velocity fields, probability density functions and power spectra of the toroidal velocity in the bulk ($r = 0.9$, $z = 0$) and near the impellers ($r = 0.9$, $z = 0.65$) can be computed (see figure 6). PDFs of the velocity at both positions are already almost Gaussian. The mean value increases with z, while the standard deviation decreases, reflecting the toroidal velocity profile generated by the impeller pumping. The power spectral density in the bulk shows a $-5/3$ slope over a range from $1f_{\mathrm{imp}}$ to $10f_{\mathrm{imp}}$ with f_{imp} the impeller rotation frequency. This is in accordance with power spectra measured in the TM60 experimental configuration [34]. The power spectrum near the impeller is dominated by impeller time scales, especially a sharp peak at $f = 8f_a$ due to the geometry with 8 blades. A comparison of small frequencies in the spectrum respectively long-term dynamics with experimental observations would require longer simulations.

Long simulations are also required to gain sufficient statistics for calculations of the global angular momentum of the fluid, defined in [58], which characterizes the flow symmetry. At sufficiently high Reynolds numbers the statistical properties of this quantity change radically, which can be seen as a phase transition of the flow. The necessary Reynolds numbers for this process are not accessible for DNSs, thus only the response of the angular momentum to forcing asymmetries at small Reynolds numbers can be analysed and compared to experimental results in future work.
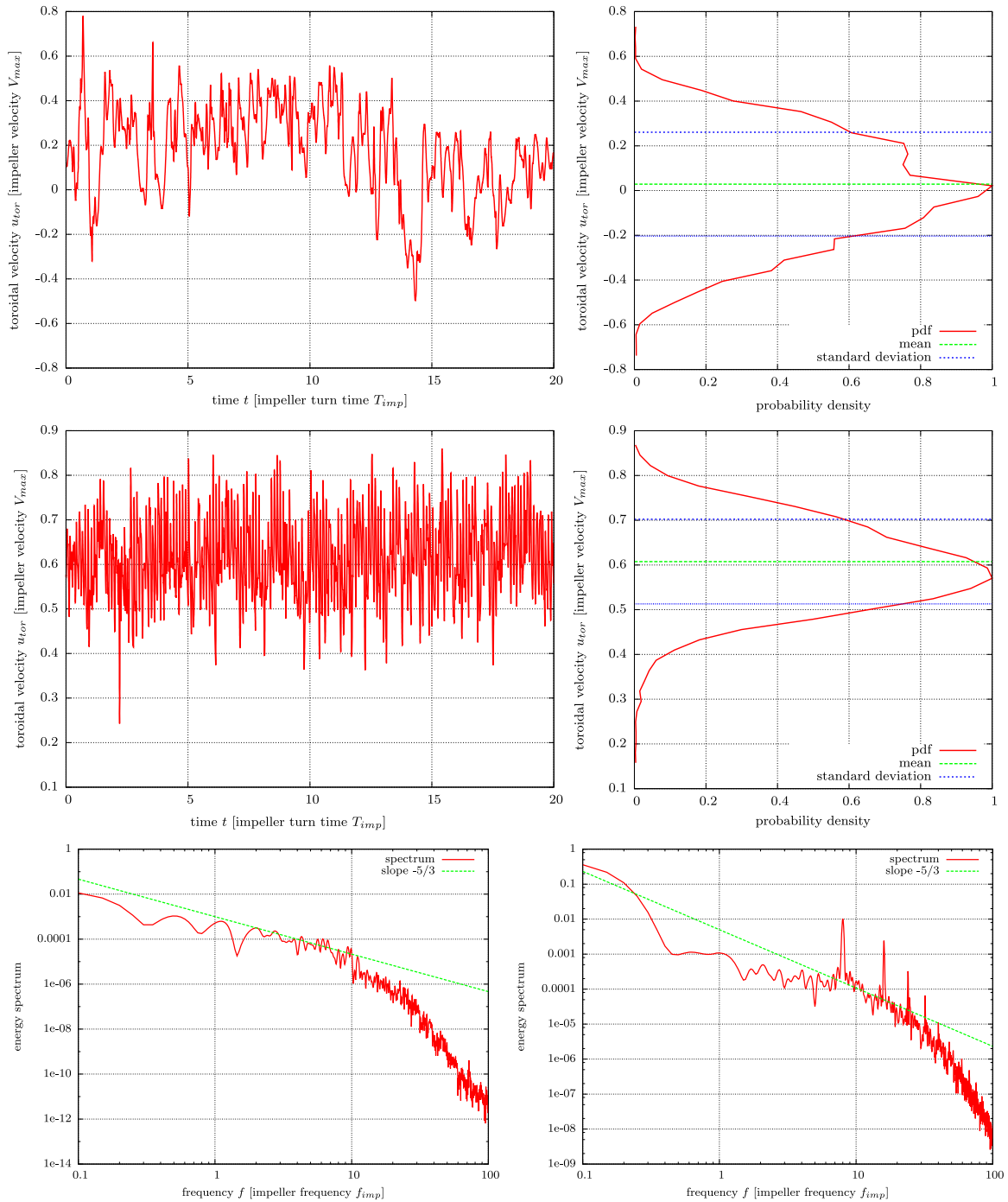
Figure 6. Temporal signal of toroidal velocity $u_{\mathrm{tor}}(t)$ at $r = 0.9$, $z = 0$ (top row) and at $r = 0.9$, $z = 0.65$ (middle row) for the (+) run at $Re = 2430$ and the related PDFs (averaged over 4 points with equal r and z). PDFs are almost Gaussian with a shift of the mean to larger values and decreased standard deviation for increasing z due to the pumping of the impellers. Power spectra for the toroidal velocity at $z = 0$ (middle of the bulk) (bottom left) and at $z = 0.65$ (near the impeller) (bottom right) have been computed using Gabor transforms with a window width of T_{imp}. While the spectrum in the bulk appears to have a slope $-5/3$, the spectrum near the impeller is dominated by impeller time scales.

In addition, when the water experiments are running during a long time, the von Kármán mean flow can change to different topology solutions, breaking symmetries [32, 34, 59]. In the experiment, the typical time scale to record this multi-stability is around 10^5–10^6 hydrodynamic large eddy turnover times. In our present simulations, we are completely out of reach to record such dynamics: we computed 20 disk turns, which represent around 45 eddy turnover times only. It would thus be very interesting to perform long numerical runs with small spatial resolutions to reach and study the long time physical behaviours or to improve statistical data. Instead of catching long-term dynamics, it could be easier to seek the symmetry breaking produced by a difference of the rotation speed of the two impellers [32], which generates hysteresis cycles. By implementing a constant torque forcing, the disappearance of the hysteresis cycle could be checked, since the two branches of the torque are connected in this case [60].

Acknowledgment

References

[1] von Kármán T 1921 Uber laminare und turbulente reibung *Z. Angew. Math. Mech.* **1** 233
[2] Dijkstra D and van Heijst G J F 1983 The flow between two finite rotating disks enclosed by a cylinder *J. Fluid Mech.* **128** 123–54
[3] Douady S, Couder Y and Brachet M E 1991 Direct observation of the intermittency of intense vorticity filaments in turbulence *Phys. Rev. Lett.* **67** 983–6
[4] Fauve S, Laroche C and Castaing B 1993 Pressure fluctuations in swirling turbulent flows *J. Phys. II* **3** 271–8
[5] Labbé R and Pinton J-F 1994 Correction to Taylor hypothesis in swirling flows *J. Phys. II (France)* **4** 1461–8
[6] Abry P, Fauve S, Flandrin P and Laroche C 1994 Analysis of pressure fluctuations in swirling turbulent flows *J. Phys. II* **4** 725–33
[7] Labbé R, Pinton J-F and Fauve S 1996 Study of the von Kármán flow between coaxial corotating disks *Phys. Fluids* **8** 914–22
[8] Mordant N, Metz P, Michel O and Pinton J-F 2001 Measurement of Lagrangian velocity in fully developed turbulence *Phys. Rev. Lett.* **87** 214501
[9] Mordant N, Delour J, Léveque E, Arnéodo A and Pinton J-F 2002 Long time correlations in Lagrangian dynamics: a key to intermittency in turbulence *Phys. Rev. Lett.* **89** 254502
[10] la Porta A, Voth G A, Moisy F and Bodenschatz E 2000 Using cavitation to measure statistics of low-pressure events in large-Reynolds-number turbulence *Phys. Fluids* **12** 1485–96
[11] la Porta A, Voth G A, Crawford A M, Alexander J and Bodenschatz E 2001 Fluid particle accelerations in fully developed turbulence *Nature* **409** 1017–9
[12] Saint-Michel B *et al* 2013 Probing quantum and classical turbulence analogy through global bifurcations in a von Karman liquid helium experiment submitted
[13] Gailitis A *et al* 2000 Detection of a flow induced magnetic field eigenmode in the Riga dynamo facility *Phys. Rev. Lett.* **84** 4365

[14] Gailitis A *et al* 2001 Magnetic field saturation in the Riga dynamo experiment *Phys. Rev. Lett.* **86** 3024

[15] Müller U and Stieglitz R 2000 Can the Earth's magnetic field be simulated in the laboratory? *Naturwissenschaften* **87** 381

[16] Stieglitz R and Müller U 2001 Experimental demonstration of a homogeneous two-scale dynamo *Phys. Fluids* **13** 561

[17] Monchaux R *et al* 2007 Generation of a magnetic field by dynamo action in a turbulent flow of liquid sodium *Phys. Rev. Lett.* **98** 044502

[18] Berhanu M *et al* 2007 Magnetic field reversals in an experimental turbulent dynamo *Europhys. Lett.* **77** 59001

[19] Monchaux R *et al* 2009 The von Kármán sodium experiment: turbulent dynamical dynamos *Phys. Fluids* **21** 035108

[20] Berhanu M *et al* 2009 Bistability between a stationary and an oscillatory dynamo in a turbulent flow of liquid sodium *J. Fluid Mech.* **641** 217–26

[21] Berhanu M *et al* 2010 Dynamo regimes and transitions in the VKS experiment *Eur. Phys. J.* B **77** 459–68

[22] Gallet B *et al* 2012 Experimental observation of spatially localized dynamo magnetic fields *Phys. Rev. Lett.* **108** 144501

[23] Marié L, Burguete J, Daviaud F and Léorat J 2003 Numerical study of homogeneous dynamo based on experimental von Kármán type flows *Eur. Phys. J. B—Condens. Matter Complex Syst.* **33** 469–85

[24] Ravelet F, Chiffaudel A, Daviaud F and Léorat J 2005 Toward an experimental von Kármán dynamo: numerical studies for an optimized design *Phys. Fluids* **17** 117104

[25] Marié L, Normand C and Daviaud F 2006 Galerkin analysis of kinematic dynamos in the von Kármán type geometry *Phys. Fluids* **18** 469–85

[26] Laval J-P, J-P, Blaineau P, Leprovost N, Dubrulle B and Daviaud F 2006 Influence of turbulence on the dynamo threshold *Phys. Rev. Lett.* **96** 204503

[27] Dubrulle B, Blaineau P, Lopes Mafra O, Daviaud F, Laval J-P and Dolganov R 2007 Bifurcations and dynamo action in a Taylor–Green flow *New J. Phys.* **9** 308

[28] Ponty Y, Laval J-P, Dubrulle B and Pinton J-F 2007 Subcritical dynamo bifurcation in the Taylor–Green-flow *Phys. Rev. Lett.* **99** 224501

[29] Reuter K, Jenko F and Forest C 2011 Turbulent magnetohydrodynamic dynamo action in spherical bounded von Kármán flow at small magnetic Prandtl numbers *New J. Phys.* **13** 073019

[30] Marié L September 2003 Transport de moment cinétique et de champ magnétique par un écoulement tourbillonnaire turbulent: influence de la rotation *Thesis* Université Paris-Diderot—Paris VII

[31] Marié L and Daviaud F 2004 Experimental measurement of the scale-by-scale momentum transport budget in a turbulent shear flow *Phys. Fluids* **16** 457

[32] Ravelet F, Marié L, Chiffaudel A and Daviaud F 2004 Multistability and memory effect in a highly turbulent flow: experimental evidence for a global bifurcation *Phys. Rev. Lett.* **93** 164501

[33] Ravelet F September 2005 Bifurcations globales hydrodynamiques et magnétohydrodynamiques dans un ecoulement de von Karman turbulent *Thesis* Ecole Polytechnique X

[34] Ravelet F, Chiffaudel A and Daviaud F 2008 Supercritical transition to turbulence in an inertially driven von Kármán closed flow *J. Fluid Mech.* **601** 339–64

[35] Shu C-W and Osher S 1988 Efficient implementation of essentially non-oscillatory shock-capturing schemes *J. Comput. Phys.* **77** 439ff

[36] Frisch U 1996 *Turbulence: The Legacy of A N Kolmogorov* (Cambridge: Cambridge University Press)

[37] Orszag S A and Patterson J S Jr 1972 Numerical simulation of three-dimensional homogeneous isotropic turbulence *Phys. Rev. Lett.* **28** 76–79

[38] Vincent A and Meneguzzi M 1991 The spatial structure and the statistical propierties of homogeneous turbulence *J. Fluid Mech.* **225** 1–25

[39] Minguez M, Pasquetti R and Serre E 2008 High-order large-eddy simulation of flow over the Ahmed body car model *Phys. Fluids* **20** 095101

[40] Homann H, Bec J and Grauer R 2013 Effect of turbulent fluctuations on the drag and lift forces on a towed sphere and its boundary layer *J. Fluid Mech.* **721** 155–79

[41] Mohd-Yusof J 1997 Combined immersed boundary/b-spline methods for simulations of flow in complex geometries *Center for Turbulence Research Annual Research Briefs* pp 317–27

[42] Fadlun E A, Verzicco R, Orlandi P and Mohd-Yusof J 2000 Combined immersed-boundary finite-difference methods for three-dimensional complex flow simulations *J. Comput. Phys.* **161** 35ff

[43] Brown D L, Cortez R and Minion M L 2001 Accurate projection methods for the incompressible Navier–Stokes equations *J. Comput. Phys.* **168** 464–99

[44] Cortet P-P, Diribarne P, Monchaux R, Chiffaudel A, Daviaud F and Dubrulle B 2009 Normalized kinetic energy as a hydrodynamical global quantity for inhomogeneous anisotropic turbulence *Phys. Fluids* **21** 025104

[45] Dudley M L and James R W 1989 Time-dependent kinematic dynamos with stationary flows *Proc. R. Soc.* A **425** 407–29

[46] Schmitt B J and von Wahl W 1992 Decomposition of solenoidal fields into poloidal fields, toroidal fields and the mean flow. Applications to the Boussinesq equations *Lect. Notes Math.* **1530** 291

[47] Cardin P and Cugliandolo L F 2008 *Dynamos, Volume Session LXXXVIII, 2007 of Les Houches—Ecole d'Ete de Physique Theorique* (Amsterdam: Elsevier)

[48] Cadot O, Douady S and Couder Y 1995 Characterization of the low pressure filaments in a three-dimensional turbulent shear flow *Phys. Fluids* **7** 630–46

[49] Mordant N, Pinton J-F and Chillà F 1997 Characterization of turbulence in a closed flow *J. Phys. II* **7** 1729–42

[50] Labbé R, Pinton J-F and Fauve S 1996 Power fluctuations in turbulent swirling flows *J. Phys. II* **6** 12

[51] Petrelis F, Mordant N and Fauve S 2007 On the magnetic fields generated by experimental dynamos *Geophys. Astrophys. Fluid Dyn.* **101** 289–323

[52] Laguerre R, Nore C, Ribeiro A, Léorat J, Guermond J-L and Plunian F 2008 Impact of impellers on the axisymmetric magnetic mode in the VKS2 dynamo experiment *Phys. Rev. Lett.* **101** 104501

[53] Giesecke A, Stefani F and Gerbeth G 2010 Role of soft-iron impellers on the mode selection in the von Kármán-sodium dynamo experiment *Phys. Rev. Lett.* **104** 044503

[54] Ravelet F, Dubrulle B, Daviaud F and Ratié P-A 2012 Kinematic α tensors and dynamo mechanisms in a von Kármán swirling flow *Phys. Rev. Lett.* **109** 024503

[55] Verhille G, Plihon N, Bourgoin M, Odier P and Pinton J-F 2010 Induction in a von Kármán flow driven by ferromagnetic impellers *New J. Phys.* **12** 033006

[56] Giesecke A, Nore C, Stefani F, Gerbeth G, Léorat J, Herreman W, Luddens F and Guermond J-L 2012 Influence of high-permeability discs in an axisymmetric model of the Cadarache dynamo experiment *New J. Phys.* **14** 053005

[57] Miralles S, Bonnefoy N, Bourgoin M, Odier P, Pinton J-F, Plihon N, Verhille G, Boisson J, Daviaud F and Dubrulle B 2013 Dynamo threshold detection in the von Kármán sodium experiment *Phys. Rev.* E **88** 013002

[58] Cortet P-P, Herbert E, Chiffaudel A, Daviaud F, Dubrulle B and Padilla V 2011 Susceptibility divergence, phase transition and multistability of a highly turbulent closed flow *J. Stat. Mech.: Theory Exp.* **2011** P07012

[59] de la Torre A and Burguete J 2007 Slow dynamics in a turbulent von Kármán swirling flow *Phys. Rev. Lett.* **99** 054101

[60] Saint-Michel B, Dubrulle B, Marié L, Ravelet F and Daviaud F 2013 Evidence for forcing-dependent steady states in a turbulent swirling flow *Phys. Rev. Lett.* **111** 234502